

## Microwave spectroscopy of calcium Rydberg states

Thomas R. Gentile,\* Barbara J. Hughey,<sup>†</sup> and Daniel Kleppner

*Research Laboratory of Electronics, Department of Physics, Massachusetts Institute of Technology,  
Cambridge, Massachusetts 02139*

Theodore W. Ducas

*Wellesley College, Wellesley, Massachusetts 02181*

(Received 2 January 1990)

We report results of a survey of microwave transition frequencies between *S*, *P*, and *D* singlet and triplet Rydberg states of calcium in the range  $n = 22-55$ . The accuracy of the measurements is approximately one part in  $10^6$ . The data have been analyzed using generalized energy expansions for the quantum defects, with the exception of the  $4snd\ ^1D_2$  series, for which numerical values of the quantum defects are presented.

### I. INTRODUCTION

Microwave spectroscopy makes it possible to determine the structure of Rydberg states of atoms with high precision.<sup>1-3</sup> A number of such studies have been carried out on alkali-metal atoms. Results include measurements of quantum defects with unprecedented precision, fine and hyperfine structure intervals, polarizabilities, and specific isotope shifts.<sup>4-6</sup> Quantum defects of alkali-metal atoms display a weak, monotonic dependence on energy. In contrast, the quantum defects of alkaline-earth atoms can vary significantly with energy because of effects due to doubly excited states. In calcium, such effects have been studied in high angular momentum states using microwave spectroscopy,<sup>7</sup> but to our knowledge the low angular momentum states have only been studied optically. We present here results of microwave measurements of transition frequencies between calcium singlet and triplet *S*, *P*, and *D* Rydberg states. The range in principal quantum number of the measurements is  $n = 22-55$  and the accuracy is typically one part in  $10^6$ . Except for the strongly perturbed  $4snd\ ^1D_2$  series, we have interpreted our results using generalized energy expansions for the quantum defects.

Calcium is intermediate in complexity among alkaline-earth atoms: several doubly excited states perturb the bound-state spectrum, but most of these lie at much lower energies than the states studied here. (The exception is the  $3d^2\ ^1D_2$  state, which is mixed into the entire  $4snd\ ^1D_2$  series.) The spectrum in the vicinity of these perturbers has been studied by optical spectroscopy.<sup>8-14</sup> Armstrong *et al.*<sup>11,13</sup> interpreted their observations using multichannel quantum-defect theory. The optical data, which yield the most accurate quantum defects at low values of  $n$ , provide information in the region where the spectrum is strongly perturbed. Our microwave measurements complement these data by providing precise measurements in the region where the spectrum is less perturbed.

In Sec. II we describe the apparatus used for these

measurements. Measurement procedures and characteristics of the spectra are described in Sec. III. The determination of quantum defects from the data is described in Sec. IV. Tables of the measured transition frequencies are presented in Appendix A.

### II. EXPERIMENT

We present only a brief description of the apparatus because many of its details have been described previously.<sup>15</sup> Rydberg atoms are produced by the following three-step pulsed laser excitation in a thermal atomic beam of calcium:  $4s^2\ ^1S_0 \rightarrow 4s4p\ ^1P_1$  (423 nm),  $4s4p\ ^1P_1 \rightarrow 4s5s\ ^1S_0$  (1034 nm), and  $4s5s\ ^1S_0 \rightarrow 4snp\ ^1P_1$  (630 nm). A schematic diagram of the apparatus is shown in Fig. 1. The atomic beam crosses the waveguide and then enters the detector, where selective field ionization is used to detect and differentiate the two Rydberg states involved in the transition. Laser excitation occurs either within the waveguide itself or before the waveguide, between the waveguide holder and the collimating plate.

In addition to the  $4snp\ ^1P_1$  states,  $4sns\ ^1S_0$  states could be excited using Stark mixing. Stark mixing was accomplished by applying a small electric field (7 V/cm for  $n \approx 46$ ) between the collimating plate and the waveguide holder.

Microwave transitions were studied in the frequency range between 26.5 and 120 GHz. The radiation was transmitted to the atoms through WR-28 waveguide (3.56 mm  $\times$  7.11 mm). The waveguide was shorted, producing a standing wave. (In studies of Rabi oscillations published elsewhere,<sup>15</sup> the shorted waveguide configuration was found to cause power-dependent shifts. However, these shifts were negligible at the lower power levels used for the spectroscopy described in this paper.) The atoms traverse the short axis of the waveguide, passing through 1.3 mm apertures that do not significantly perturb the field. The aperture in the collimating plate restricts the atomic-beam diameter to 0.5 mm. The laser beams inter-

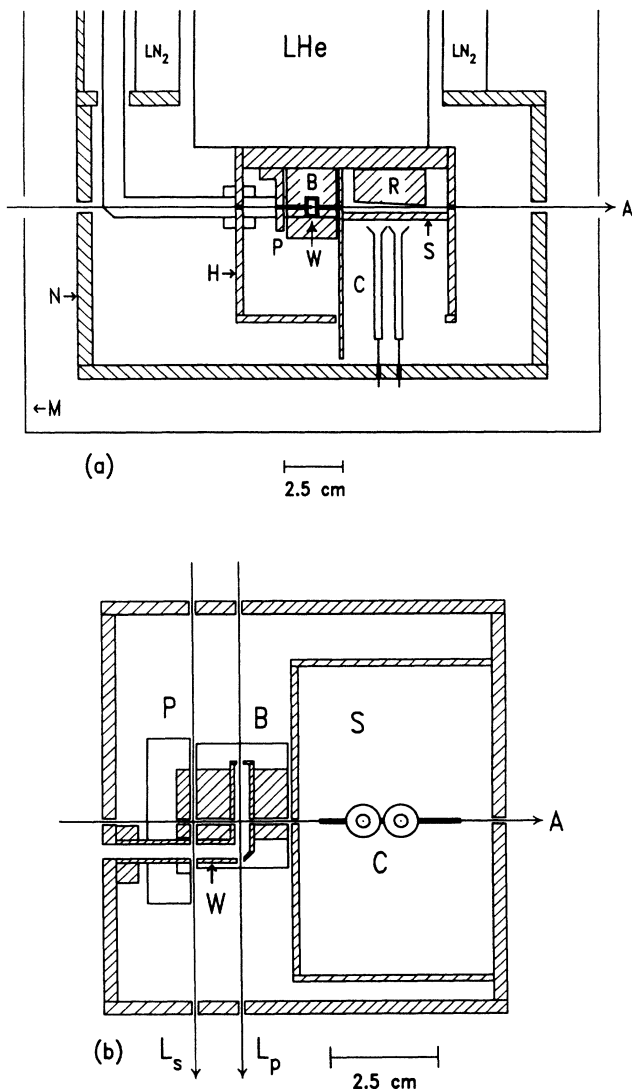


FIG. 1. Diagrams of the apparatus. (a) Side view of the system. *A*, atomic beam; *P*, collimating plate; *W*, waveguide; *B*, waveguide holder; *R*, ramped electric field plate; *S*, slotted electric field plate; *C*, channel electron multipliers; *H*, radiation shield connected to the liquid-helium reservoir; *N*, radiation shield connected to the liquid-nitrogen reservoir; *M*, magnetic shield. (b) View from below.  $L_p$ , path of laser beams for  $4snp\ ^1P_1$  excitation;  $L_s$ , path of laser beams for  $4sns\ ^1S_0$  excitation.

sect the atomic beam 1.2 mm from the waveguide entrance, resulting in a mean transit time to the exit of 3  $\mu$ sec.

The microwave source is a 26.5–40-GHz sweep oscillator which is phase locked to a harmonic of the output of a frequency synthesizer. The synthesizer was calibrated against a rubidium frequency standard. The range of the microwave source was extended to 120 GHz by harmonic generation. Consequently, the frequencies of our measurements lie in three ranges: fundamental (26.5–40 GHz), second harmonic (53–80 GHz), and third harmonic (79.5–120 GHz). Since the conversion efficiency of the

harmonic generator is low, residual radiation from below the desired harmonic is a potential source of ac Stark shifts. We eliminated such radiation using waveguide filters.

For the fundamental frequency range the waveguide supports only the  $TE_{10}$  mode, which has a constant electric field along the atomic-beam axis. However, for the harmonic ranges other modes can be present.

### III. TRANSITION FREQUENCY MEASUREMENTS

#### A. Measurement procedures and transition characteristics

Figure 2 is an energy level diagram that illustrates the various types of transitions that we studied. The measured transition frequencies are listed in Tables IV–XII in Appendix A. The difference between a measured frequency and the frequency calculated from the quantum-defect analysis described in Sec. IV—referred to as the “residual”—is listed for each transition.

For transitions starting from  $4snp\ ^1P_1$  states, the atoms were excited by the laser beams within the waveguide. The microwave power was turned on 0.02–0.1  $\mu$ sec after the laser pulse and left on for 5–10  $\mu$ sec. Because the mean transit time was 3  $\mu$ sec, most of the atoms interacted with the microwaves for the entire time they were in the waveguide. This resulted in a 300-kHz transit time linewidth [full width at half maximum (FWHM)]. For transitions starting from the  $4sns\ ^1S_0$  states, the atoms were excited in front of the waveguide. The microwave

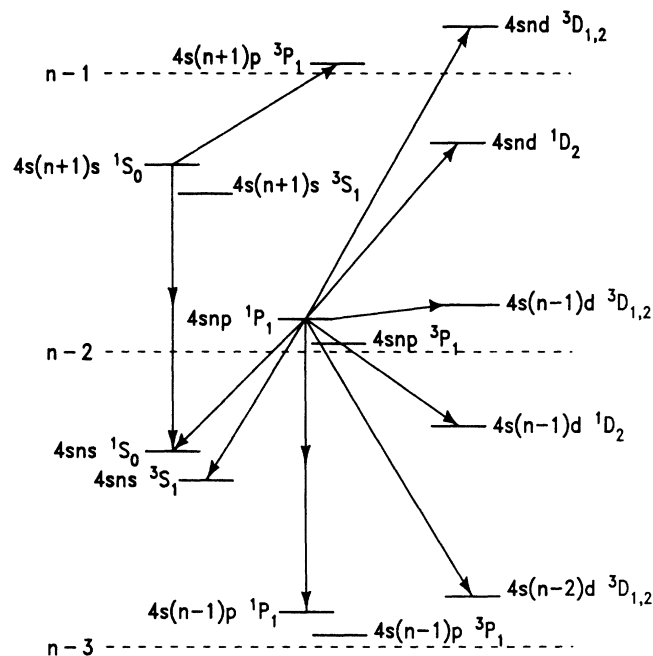


FIG. 2. Energy-level diagram of calcium illustrating the types of transitions studied in this paper. The dashed lines indicate the location of levels with zero quantum defect. The quantum defects of the states shown are  $\delta(^1S_0)=2.34$ ,  $\delta(^1P_1)=1.88$ ,  $\delta(^1D_2)=1.26$  (at  $n=50$ ),  $\delta(^3S_1)=2.44$ ,  $\delta(^3P_1)=1.96$ , and  $\delta(^3D_{1,2})=0.83$ .

power was on continuously, yielding a transit time linewidth of 200 kHz.

Figure 3 shows a typical experimental resonance and the calculated line shape. The line shape was calculated by averaging the transition probability over the velocity spread of the thermal atomic beam. The centers of the resonances were found by the time-honored technique of splitting the line by eye: the signal-to-noise ratio was not high enough to justify a more sophisticated analysis. The statistical uncertainty in locating the line center was approximately  $\pm 7\%$  of the FWHM. The statistical uncertainty and uncertainty related to line shape that are discussed below will be referred to as "measurement uncertainty."

The observed width of the resonances was usually the transit time linewidth. Other potential broadening sources include the Doppler effect, noise in the microwave source, natural linewidth, and power broadening. These were all negligible except for the natural linewidth of  $4snp\ ^1P_1 \rightarrow 4sn'd\ ^1D_2$  transitions at low values of  $n'$ : for our lowest transition ( $4s26p\ ^1P_1 \rightarrow 4s25d\ ^1D_2$ ) the natural linewidth is expected to be  $\approx 300$  kHz.<sup>16</sup> Power broadening was avoided by attenuating the microwave power until only 10% transfer of the population was observed. For the  $4snp\ ^1P_1 \rightarrow 4sn'd\ ^1D_2$  and three  $4snp\ ^1P_1 \rightarrow 4s(n-1)d\ ^3D_J$  transitions, however, the final states could not be observed because of their short lifetimes. These transitions were detected by measuring the depletion of the population of the initial  $4snp\ ^1P_1$  state. In this case, the transfer was increased to 30% to improve the signal-to-noise ratio.

The linewidths for most of the harmonic transitions were usually equal to the transit time linewidth, though a few were as much as twice the transit time linewidth. Such broadening could be expected because the transit

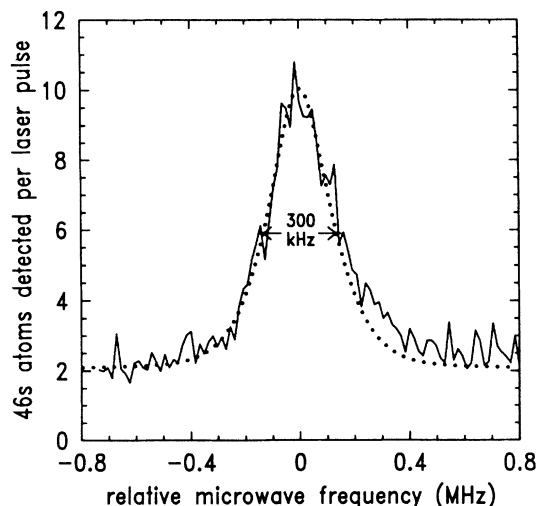


FIG. 3. The experimental resonance for the  $4s46p\ ^1P_1 \rightarrow 4s46s\ ^1S_0$  transition. The frequency is measured relative to 35.331 936 GHz. The dotted line is the calculated line shape, as described in the text.

time line shape is affected by the presence of higher-order waveguide modes. Since these line shapes are not as well understood as those for the fundamental transitions, we assigned them a fractional measurement uncertainty double that of the fundamental transitions. The reproducibility of these measurements and the scatter of the residuals for these data are consistent with these estimated uncertainties.

Of the 67 harmonic transitions observed, 13 exhibited an anomalous line shape consisting of three to seven peaks separated by 600 kHz. Studies of the harmonic microwave spectrum revealed no sidebands that could explain these line shapes.<sup>17</sup> Another possibility might be an effect of higher-order modes in the waveguide. However, we could not explain these anomalous line shapes using any plausible mode structure. We tested the effect of excluding these anomalous transitions from our quantum-defect analysis, and found that the final results were shifted only by amounts that were small compared to their uncertainties. Thus we do not believe any pathological problems arise from these transitions, despite the uncomfortable fact that we do not understand them. We included these transitions in the final analysis, but assigned them uncertainties equal to the spread of their multi-peaked structures. We believe these uncertainties are quite conservative because the residuals for these data are much smaller than these uncertainties.

In two other transitions ( $4s39p\ ^1P_1 \rightarrow 4s39s\ ^3S_1$  and  $4s35s\ ^1S_0 \rightarrow 4s35p\ ^3P_1$ ) we observed two partially resolved peaks separated by 300 and 200 kHz, respectively. As with the anomalous line shapes, we have no theory for the line structure. Consequently, we assigned them an uncertainty that encompassed both peaks.

The microwave intensity was typically  $\sim 10^{-13}$  W/cm<sup>2</sup> for a one-photon singlet-singlet transition,  $\sim 10^{-8}$  W/cm<sup>2</sup> for a two-photon transition, and  $\sim 10^{-9}$  W/cm<sup>2</sup> for a one-photon singlet-triplet transition. These intensities were measured on transitions in the fundamental range of frequencies, for which the waveguide mode structure is known. The measurements were consistent with calculations based on earlier studies of one- and two-photon Rabi oscillations,<sup>15</sup> and estimates of the singlet-triplet mixing coefficients.<sup>13</sup>

## B. Systematic errors

### 1. Stark shifts

The most important source of systematic error in these measurements is the Stark shift from stray electric fields. This is the only effect which required corrections to the data. However, these corrections were often much smaller than the linewidth and rarely exceeded half the linewidth.

The states we studied have large quantum defects and consequently do not display first-order Stark shifts in low fields. However, the second-order Stark shift can be significant. The second-order Stark shift coefficients of the transitions we studied were mainly between 10 and 1000 MHz/(V/cm)<sup>2</sup>. These coefficients were calculated from second-order perturbation theory using computed

matrix elements and our measured transition frequencies. Because the second-order Stark shift scales as  $n^7$ , the stray field can be diagnosed by examining the characteristics of transitions at high  $n$ . We probed the stray field using the  $4s74p\ ^1P_1 \rightarrow 4s75d\ ^1D_2$  and  $4s55p\ ^1P_1 \rightarrow 4s55d\ ^1D_2$  transitions. By an analysis described elsewhere,<sup>17</sup> we estimated both the magnitude and direction of the stray electric field. From day to day the magnitude varied between 12 and 25 mV/cm. The field information was used to correct each transition frequency. The Stark shift corrections and their uncertainties are listed with the transition frequencies in the tables in Appendix A. The uncertainties in these corrections are due to the uncertainties in the knowledge of the stray field on the day each transition was performed. The contribution of the Stark shift uncertainties to the total uncertainties was typically smaller than or comparable to the measurement uncertainties, although for a few transitions at high  $n$  it was as much as four times larger. The systematic effect of the field on the final evaluation of the quantum defects is small, as will be discussed in Sec. IV B.

## 2. Zeeman and ac Stark shifts

Effects of Zeeman splitting were reduced by employing a single-layer  $\mu$ -metal magnetic shield and constructing the apparatus from nonmagnetic materials. The residual magnetic field in the waveguide,  $6(\pm 4)$  mG, caused a maximum splitting of 28 kHz between the  $m = +1$  and  $m = -1$  sublevels of a  $4snp\ ^1P_1$  state, which is less than 10% of the transit time linewidth. In addition, because the residual magnetic field was essentially perpendicular to the microwave field, the dominant effect was to split, rather than shift, a transition.

The ac Stark shift is a potential source of concern for two-photon transitions and singlet-triplet transitions because of the higher power levels required. However, we did not observe frequency shifts for modest increases in the microwave power. This is consistent with estimates of the magnitude of ac Stark shifts at the power levels used for these measurements.

## IV. QUANTUM-DEFECT ANALYSIS

### A. Spectra of alkaline-earth atoms

Spectroscopic data on weakly perturbed Rydberg series are most conveniently analyzed in terms of generalized energy expansions of the quantum defects for each series. However, the procedures that we employed were not entirely straightforward because the most successful strategy for extracting quantum defects required a simultaneous fit of all the data. We found that two different representations are useful: a generalized energy expansion (Langer's formula<sup>18</sup>) and an approximation to this expansion that recovers a simple power series in the energy. Each form has its advantages, as the following discussion demonstrates.

The energy levels of alkali-metal atoms are well described by the formula

$$E_n = \frac{-1}{2(n-\delta)^2} \quad (1)$$

(atomic units<sup>19</sup>). The quantum defect  $\delta$  depends strongly on the orbital quantum number  $l$  but varies only weakly with the energy. We will expand this variation as a power series in the reduced energy variable  $\epsilon_n \equiv [n - \delta(\epsilon_n)]^{-2} = -2E_n$ :

$$\delta(\epsilon_n) = \delta_0 + \delta_1\epsilon_n + \delta_2\epsilon_n^2 + \dots \quad (2)$$

For Rydberg states of alkali-metal atoms only the linear term in  $\epsilon_n$  is usually necessary to describe the spectra accurately.

Because alkaline-earth atoms have two valence electrons, configuration interaction can complicate their spectra. In calcium, configuration mixing arises primarily from the electrostatic interaction of the two valence electrons. The electrostatic Hamiltonian commutes with  $J$ ,  $L$ ,  $S$ , and parity, hence only configurations with the same values of these quantum numbers can interact.

The effect of a perturbing state  $|p\rangle$  on the quantum defect of a Rydberg state is to introduce an additional term in the expansion of the quantum defect:

$$\delta(\epsilon_n) = \delta'_0 + \delta'_1\epsilon_n + \dots + \frac{\alpha}{\epsilon_n^0 - \epsilon_p^0} \quad (3)$$

where  $\epsilon_n^0$  and  $\epsilon_p^0$  are the unperturbed reduced energies of the Rydberg and perturbing states, respectively. This expression, which was originally derived by Langer,<sup>18</sup> has been discussed by a number of authors.<sup>20-22</sup> [The primed notation is a reminder that the coefficients of corresponding powers of  $\epsilon_n$  in Eqs. (2) and (3) are not identical.] In practice it is often convenient to evaluate  $\delta(\epsilon_n)$  using the observed reduced energies  $\epsilon_n$  and  $\epsilon_p$ , rather than  $\epsilon_n^0$  and  $\epsilon_p^0$ ; this presents no problems because  $|\epsilon_n - \epsilon_n^0|, |\epsilon_p - \epsilon_p^0| \ll |\epsilon_n - \epsilon_p|$ .

In the energy range where a series is strongly perturbed, multichannel quantum-defect theory<sup>23</sup> provides the best description of the system. However, far from perturbing states Eq. (3) is often adequate. Except for the  $3d^2\ ^1D_2$  state, all the perturbers we are concerned with in calcium are located below  $n \approx 10$ . Thus for the range of our measurements ( $n \geq 22$ ) this approach is valid for all the series we studied except the  $4snd\ ^1D_2$  series.

Although the quantum defects of many Rydberg series in calcium can be accurately described by Eq. (3), another approach is useful. Since the perturbing states are much more tightly bound than the Rydberg states, we can expand the last term in Eq. (3) as

$$\frac{\alpha}{\epsilon_n - \epsilon_p} = \frac{-\alpha}{\epsilon_p} \left[ 1 + \frac{\epsilon_n}{\epsilon_p} + \left( \frac{\epsilon_n}{\epsilon_p} \right)^2 + \dots \right]. \quad (4)$$

(Note that we have used the observed reduced energies  $\epsilon_n$  rather than the unperturbed reduced energies  $\epsilon_n^0$ .) Thus we have recovered a power-series expansion in  $\epsilon_n$ :

$$\delta(\epsilon_n) = \sum_{i=0}^{\infty} \delta_i(\epsilon_n)^i, \quad (5)$$

where

$$\delta_i = \delta'_i - \frac{\alpha}{\epsilon_p} \frac{1}{(\epsilon_p)^i} \quad (5a)$$

This approach continues to be valid if there is more than one perturber. Often the major effect of the perturber is to shift  $\delta_0$  and introduce a linear variation with energy of the quantum defect. In this case Eq. (5) is better suited to fitting the quantum defect than Eq. (3), because the latter separates the linear dependence into two parts.

We can rewrite Eqs. (3) and (5) explicitly in terms of  $n$  by approximating  $\epsilon_n$  by the leading order term in the quantum-defect expansion. Such an approximation is not necessarily valid if the series is strongly perturbed, but no improvements in our results were obtained by using a more precise approximation to the energy. The final forms we used to fit our data are thus

$$\delta(n) = \delta'_0 + \frac{\delta'_1}{(n - \delta'_0)^2} + \cdots + \frac{\alpha}{(n - \delta'_0)^{-2} - \epsilon_p} \quad (6)$$

and

$$\delta(n) = \delta_0 + \frac{\delta_1}{(n - \delta_0)^2} + \frac{\delta_2}{(n - \delta_0)^4} + \cdots \quad (7)$$

Equations (6) and (7) will be referred to as the “perturber” and “pure power-series” forms, respectively. The quantum defect is conventionally labeled with a subscript that designates the orbital angular momentum  $l$  of the series. For the alkaline-earth series three subscripts ( $L$ ,  $S$ , and  $J$ ) are required for a complete identification. However, to simplify the notation we will display such subscripts only when necessary to avoid confusion.

### B. Data analysis

We have used our spectroscopic measurements to extract the quantum defects of the following series in ranges extending from  $22 \leq n \leq 55$ :  $4snp \ ^1P_1$ ,  $4sns \ ^1S_0$ ,  $4sns \ ^3S_1$ ,  $4snp \ ^3P_1$ ,  $4snd \ ^3D_1$ ,  $4snd \ ^3D_2$ , and  $4snd \ ^1D_2$ . The bound-state perturbers for these series are listed in Table I. Perturbers also exist in the continuum, but they need not be explicitly included to fit the data.

TABLE I. Bound-state perturbers in calcium for the Rydberg series studied, from Sugar and Corliss.<sup>a</sup>  $I = 49\,305.95 \text{ cm}^{-1}$  is the ionization limit,  $R = 109\,735.81 \text{ cm}^{-1}$  is the Rydberg constant for calcium. As defined in the text,  $\epsilon_p \equiv -2E_p$ , where  $E_p$  is the energy in atomic units.

Series	Perturbers	$I - R\epsilon_p$ ( $\text{cm}^{-1}$ )	$\epsilon_p$
$4snp \ ^1P_1$	$3d4p \ ^1P_1$	43 933.477	0.048 958 25
$4sns \ ^1S_0$	$4p^2 \ ^1S_0$	41 786.276	0.068 525 25
$4sns \ ^3S_1$	No perturbers		
$4sns \ ^3P_1$	$3d4p \ ^3P_1$	39 335.322	0.090 860 29
$4snd \ ^3D_1$	$3d5s \ ^3D_1$	47 456.452	0.016 854 10
$4snd \ ^3D_2$	$3d5s \ ^3D_2$	47 466.014	0.016 767 00
$4snd \ ^1D_2$	$3d5s \ ^1D_2$	47 449.083	0.016 921 25
	$4p^2 \ ^1D_2$	40 719.847	0.078 243 40
	$3d^2 \ ^1D_2$	Configuration mixed into entire series	

<sup>a</sup>Reference 25.

The transition frequencies are of the form

$$\nu = \frac{cR}{[n - \delta(n)]^2} - \frac{cR}{[(n-1) - \delta(n-1)]^2} \quad (\text{two photon}) \quad (8)$$

and

$$\nu = \frac{cR}{[n - \delta_{LSJ}(n)]^2} - \frac{cR}{[n' - \delta_{L'S'J'}(n')]^2} \quad (\text{one photon}), \quad (9)$$

where  $cR = 3.289\,796\,82 \times 10^6 \text{ GHz}$  for calcium. (The Rydberg constant for calcium is  $R = 109\,735.81 \text{ cm}^{-1}$ .) All of the data except those for the  $4snp \ ^1P_1 \rightarrow 4sn'd \ ^1D_2$  transitions were fit to Eqs. (8) or (9) using the quantum-defect expansions in Eqs. (6) and/or (7). We varied the fitting parameters for all the series using a nonlinear algorithm<sup>24</sup> to obtain the best fit for the complete set of data. Each transition frequency was weighted according to its measurement uncertainty. The resulting parameters are presented in Table II and the residuals are listed with the data in Appendix A. The particular choice of quantum-defect expansion [Eq. (6) or (7)] depended on the nature of the quantum defects for each series. The  $4sns \ ^1S_0$ ,  $4sns \ ^3S_1$ , and  $4snp \ ^3P_1$  series were fit precisely to the pure power-series expansion using the terms  $\delta_0$  and  $\delta_1$ . The  $4snp \ ^1P_1$  series, which is more strongly perturbed, was fit precisely by the terms  $\delta_0$ ,  $\delta_1$ , and  $\delta_2$ . The perturber form was selected for the  $4snd \ ^3D_{1,2}$  series because the  $n$ -dependence of their quantum defects is dominated by their perturbers (note the small values of  $\delta'_i$ ). Terms up to  $\delta_3$  would be required in the pure power-series form. For the quantum defects fit by Eqs. (6) and (7), the largest  $n$  dependence is found in the  $4snd \ ^3D_{1,2}$  series

TABLE II. Fitting parameters extracted from quantum-defect analysis of data. Quantum-defect expansions are defined in Eqs. (6) and (7).

Series	Fitting parameters	Total uncertainty
$4snp \ ^1P_1$	$\delta_0 = 1.885\,584\,37$ $\delta_1 = -3.240\,869$ $\delta_2 = -23.75$	$3 \times 10^{-6}$ 0.005 2.5
$4sns \ ^1S_0$	$\delta_0 = 2.337\,930\,16$ $\delta_1 = -0.114\,284$	$3 \times 10^{-6}$ 0.003
$4sns \ ^3S_1$	$\delta_0 = 2.440\,955\,74$ $\delta_1 = 0.349\,501$	$3 \times 10^{-6}$ 0.003
$4snp \ ^3P_1$	$\delta_0 = 1.964\,709\,45$ $\delta_1 = 0.227\,641$	$3 \times 10^{-6}$ 0.003
$4snd \ ^3D_1$	$\delta'_0 = 0.883\,343\,94$ $\delta'_1 = -0.024\,534$ $\alpha = 8.511\,8398 \times 10^{-4}$	$5 \times 10^{-4}$ 0.04 $9 \times 10^{-6}$
$4snd \ ^3D_2$	$\delta'_0 = 0.885\,850\,26$ $\delta'_1 = 0.126\,493$ $\alpha = 9.075\,453\,1 \times 10^{-4}$	$5 \times 10^{-4}$ 0.04 $9 \times 10^{-6}$

TABLE III. Quantum defects of the  $4snd\ ^1D_2$  states, obtained from the quantum-defect expansion for the  $4snp\ ^1P_1$  series given in Table II and the  $4snp\ ^1P_1 \rightarrow 4sn'd\ ^1D_2$  frequency measurements. Because this series is strongly perturbed, we have not fit these quantum defects to Langer's formula. Each total uncertainty listed is the sum of the uncertainty in the  $4snp\ ^1P_1$  quantum defect ( $\Delta\delta = 1.1 \times 10^{-6}$ ) and the uncertainty in the  $4snd\ ^1D_2$  quantum defect associated with the total uncertainty in the  $4snp\ ^1P_1 \rightarrow 4sn'd\ ^1D_2$  frequency measurement, added in quadrature. It is dominated by the uncertainty in the  $4snp\ ^1P_1$  quantum defects except at high  $n$ , where the Stark shift uncertainty dominates, and for transitions with anomalous line shapes, where the measurement uncertainty dominates.

$n$	$\delta$	Total uncertainty (units of $10^{-6}$ )
55	1.271 3727	3.2
54	1.270 1133	2.6
53	1.268 7751	2.3
52	1.267 3542	2.0
51	1.265 8411	1.9
50	1.264 2279	1.8
49	1.262 5077	1.6
46	1.256 5897	1.2
45	1.254 3235	1.2
44	1.251 8849	1.2
43	1.249 2571	1.2
42	1.246 4193	1.2
41	1.243 3487	1.2
40	1.240 0193	1.2
39	1.236 4006	1.2
38	1.232 4698	5.6 <sup>a</sup>
37	1.228 1557	7.1 <sup>a</sup>
36	1.223 4440	1.2
35	1.218 2727	1.1
34	1.212 5799	4.1 <sup>a</sup>
33	1.206 2960	3.8 <sup>a</sup>
32	1.199 3386	3.5 <sup>a</sup>
31	1.191 6109	1.2
30	1.183 0017	1.1
29	1.173 3802	4.4 <sup>a</sup>
28	1.162 5950	5.0 <sup>a</sup>
27	1.150 4678	3.4 <sup>a</sup>
26	1.136 7962	1.1
25	1.121 3494	1.1

<sup>a</sup>Anomalous line shapes (see Sec. III A).

$[\delta(55) - \delta(25) = 5 \times 10^{-3}]$ , and the smallest  $n$  dependence is in the  $4sns\ ^1S_0$  series  $[\delta(55) - \delta(25) = 2 \times 10^{-4}]$ . In contrast, the quantum defects of the  $4snd\ ^1D_2$  series vary by 0.15 over this range of  $n$ 's (see Table III).

A slight discrepancy is apparent in the  $4snp\ ^1P_1 \rightarrow 4sn'd\ ^3D_2$  data for  $n = 46-52$  (Table X): nearly all of these data points are  $\sim 50$  kHz below the fit. We do not know whether this disagreement is physically significant. It is possible that the relatively large Stark shift uncertainties are the source of this discrepancy.

Two sources contribute to the uncertainties in the fitting parameters: statistical uncertainty from the least-squares fit of the transition frequencies and systematic uncertainty in the frequencies due to the stray electric

field. The statistical uncertainty was corroborated by randomly varying all the measured frequencies by amounts comparable to the measurement uncertainties and refitting the data. The variations in the fitting parameters were found to be comparable to their statistical uncertainties. To evaluate the effect on the quantum defects of the uncertainty in the stray field, the fitting procedure was carried out not only for the most probable value of the stray field, but also for the limiting values. The uncertainty in the fitting parameters due to the stray field is the variation obtained by this process. The two sources were added in quadrature to obtain the total uncertainty listed in Table II. The statistical uncertainty dominates the total uncertainty.

The fitting parameters for all of the series are highly correlated. The uncertainty listed for a given parameter is the maximum allowable variation of that parameter assuming all the other parameters are refit to accommodate the variation. The allowable variation for any given parameter with all the others fixed is much smaller than the stated uncertainty, especially for the perturber form. Consequently, all of the digits we have included are necessary to reproduce our calculated frequencies.

The  $4snd\ ^1D_2$  series is strongly perturbed and requires a multichannel quantum-defect analysis. Such an analysis of optical data has been performed by Armstrong *et al.*<sup>11</sup> Their results show that the spectrum is perturbed by the  $4p^2\ ^1D_2$ ,  $3d5s\ ^1D_2$ , and  $3d^2\ ^1D_2$  states. For our range of  $n$ , the strongest perturbation is from the  $3d^2\ ^1D_2$  state. This configuration is mixed throughout the entire  $4snd\ ^1D_2$  series and cannot be assigned to a specific energy level. We have determined the quantum defects of many of the  $4snd\ ^1D_2$  states using our values for the  $4snp\ ^1P_1$  quantum defects and the  $4snp\ ^1P_1 \rightarrow 4sn'd\ ^1D_2$  frequency measurements. The results are listed in Table III. The quantum defects are consistent with those obtained from optical data.<sup>11,13</sup>

Because fitting correlated sets of data is prone to systematic errors, it is important to investigate the validity of the analysis. In particular, it is essential to determine whether the parameters generated by the fitting procedure are unique. In principle, the quantum defects for the  $4snp\ ^1P_1$  states could be determined solely from a fit of the  $4snp\ ^1P_1 \rightarrow 4s(n-1)p\ ^1P_1$  intervals. The quantum defects of the other states could then be obtained from Eq. (9). This approach was used by Fabre *et al.*<sup>4</sup> and Goy *et al.*<sup>5,6</sup> to analyze their measurements of transition frequencies in the alkali-metal atoms. However, we could not extract the small  $\delta_2$  term in the  $4snp\ ^1P_1$  expansion from the  $4snp\ ^1P_1 \rightarrow 4s(n-1)p\ ^1P_1$  intervals alone. Consequently, we found that a better method was to fit *all* of the data simultaneously by varying the fitting parameters for all of the series. The constraints provided by simultaneously fitting all the data allowed extraction of the  $\delta_2$  term.

### C. Extrapolation of the quantum defects

Our expressions for the quantum defects should be reliable for values of  $n$  above our range of measurements because the effects of higher-order terms that are unobserv-

able in our data decrease with  $n$ . (Possible higher-order terms due to perturbers in the continuum are not expected to become important because these perturbers are much farther in energy from our range of measurements than is the ionization limit.) For values of  $n$  below our range of measurements, however, the accuracy of our quantum defects will ultimately be limited by the effect of higher-order terms which cannot be extracted from our data. The existing optical data can reveal large perturbations at low  $n$ , but their relatively low accuracy prohibits the detection of small-higher-order corrections. Nevertheless, the optical measurements can provide a check on the overall consistency of our expressions.

To avoid systematic effects associated with the evaluation of the ionization limit from the optical data, we have chosen to compare the intervals between adjacent states of a given series calculated from our quantum defects with predictions from optical data. Our results agree with optical data for  $n \geq 12$ . Below  $n \approx 12$  our results start to diverge from the optical data: such behavior is expected because in this regime the perturbation approach begins to break down.

The pure power-series form is more natural than the perturber form for the  $4snp\ ^1P_1$  series in the range of  $n$  that we have studied because the energy dependence of the quantum defect is dominated by the  $\delta_1$  term. However, the perturber form is expected to be more reliable for extrapolation to low  $n$  because the higher-order terms truncated from the pure power-series form are more significant at lower  $n$ . The perturber form also explicitly separates out the effect of the perturber. Hence we have also fit the  $4snp\ ^1P_1$  series with the perturber form. As expected, for the  $4snp\ ^1P_1$  series the agreement with the optical data for  $n \approx 12$  is slightly better for the perturber form than for the pure power-series form. Because of correlations, the parameters for the other series are slightly modified if the perturber form is used. We have listed this complete set of fitting parameters in Table XIII

in Appendix B. For the  $4sns\ ^1S_0$  and  $4snp\ ^3P_1$  series the effects of their perturbers were too small to allow accurate extraction of the perturber term.

The  $4snd\ ^1D_2$  series and  $4snd\ ^3D_2$  series cross and become slightly mixed in the vicinity of  $n \approx 15$ .<sup>14</sup> The effect of this perturbation in our range of study was not large enough to be established reliably by our analysis of the  $4snd\ ^3D_2$  series. The extrapolation of our quantum defects for this series in the vicinity of  $n = 15$  is limited by the influence of this mixing.

#### D. Summary

We have extracted quantum defects for the following Rydberg series of calcium in ranges extending from  $22 \leq n \leq 55$ :  $4snp\ ^1P_1$ ,  $4sns\ ^1S_0$ ,  $4sns\ ^3S_1$ ,  $4snp\ ^3P_1$ ,  $4snd\ ^3D_1$ ,  $4snd\ ^3D_2$ , and  $4snd\ ^1D_2$ . Simple expressions for the quantum defects for all of the series except the  $4snd\ ^1D_2$  have been obtained by simultaneously varying the fitting parameters for all of these series. We have used the pure power-series form [Eq. (7)] for all these series except the  $4snd\ ^3D_{1,2}$ , where we used the perturber form [Eq. (6)]. The  $4snp\ ^1P_1$  series was also fit using the perturber form. The results agree with optical data for  $n \geq 12$ .

The  $4snd\ ^1D_2$  series is strongly perturbed and requires a multichannel quantum-defect theory analysis. Quantum defects for this series were derived directly from the data on the  $4snp\ ^1P_1 \rightarrow 4sn'd\ ^1D_2$  transitions and our results for the  $4snp\ ^1P_1$  quantum defects.

#### ACKNOWLEDGMENTS

We acknowledge helpful discussions with W. E. Cooke. This work was supported by the Joint Services Electronics Program under Grant No. DAAL03-89-C-0001. Earlier research was supported by the Office of Naval Research (Grant No. N00014-79-C) and the National Science Foundation (Grant No. PHY84-11483).

TABLE IV.  $4snp\ ^1P_1 \rightarrow 4s(n-1)p\ ^1P_1$  transitions.

$n$	Transition frequency ( $\nu_m$ , GHz)	Stark shift (kHz)	Stark shift uncertainty (kHz)	Measurement uncertainty (kHz)	Total uncertainty (kHz)	Residual ( $\nu_m - \nu_c$ ) (kHz)
52	53.877 305	...	...	15	15	12
51	57.270 936	...	...	15	15	12
50	60.955 663	...	...	15	15	13
49	64.963 360	...	...	15	15	4
48	69.330 221	...	...	15	15	6
47	74.097 386	...	...	15	15	4
46	79.311 791	...	...	15	15	8
45 <sup>a</sup>	85.027 129	...	25	40	47	-1
44 <sup>a</sup>	91.305 046	...	20	40	45	0
43 <sup>a</sup>	98.216 474	...	20	40	45	5
42 <sup>a</sup>	105.843 379	...	15	40	43	10
41 <sup>a</sup>	114.280 751	...	15	40	43	-18
36 <sup>a</sup>	173.231 712	...	5	60	60	7

<sup>a</sup>These frequencies were obtained by summing our measurements of the  $4snp\ ^1P_1 \rightarrow 4s(n-1)d\ ^1D_2$  and  $4s(n-1)p\ ^1P_1 \rightarrow 4s(n-1)d\ ^1D_2$  transition frequencies. The Stark shift information is tabulated with those measured frequencies.

TABLE V.  $4sns\ ^1S_0 \rightarrow 4s(n-1)s\ ^1S_0$  transitions.

$n$	Transition frequency ( $\nu_m$ , GHz)	Stark shift (kHz)	Stark shift uncertainty (kHz)	Measurement uncertainty (kHz)	Total uncertainty (kHz)	Residual ( $\nu_m - \nu_c$ ) (kHz)
52	55.385 530	...	...	10	10	-6
51	58.908 102	...	...	10	10	-2
50	62.735 842	...	...	10	10	-5
49	66.902 548	...	...	10	10	6
48	71.446 566	...	...	10	10	2
47	76.411 604	...	...	10	10	6
42	109.582 120	...	...	50	50	20
41	118.426 256	...	...	1400 <sup>a</sup>	1400	9
40	128.248 352	...	...	1400 <sup>a</sup>	1400	0
39	139.187 405	...	...	40	40	-34
38	151.406 924	...	...	40	40	3

<sup>a</sup>Anomalous line shapes (see Sec. III A).

#### APPENDIX A

Tables IV–XII present the measured frequencies of all the transitions studied. The following information is included. Transition frequency  $\nu_m$ : the reported value includes the Stark shift correction. Stark shift: a positive (negative) value for the shift indicates a blue (red) shift and thus the corrected frequency  $\nu_m$  is lower (higher) than the actual measured value. No value in this column indicates that the Stark shift is negligible. Stark shift un-

certainty: uncertainty in the Stark shift correction. Measurement uncertainty: uncertainty in determining the line center of the observed resonances, as discussed in Sec. III A. Total uncertainty: sum of the Stark shift uncertainty and the measurement uncertainty added in quadrature. Residual: measured frequency ( $\nu_m$ ) minus frequency calculated from quantum-defect expansions given in Table II ( $\nu_c$ ). All uncertainties have an implied “ $\pm$ ” preceding them.

TABLE VI.  $4snp\ ^1P_1 \rightarrow 4sns\ ^1S_0$  transitions.

$n$	Transition frequency ( $\nu_m$ , GHz)	Stark shift (kHz)	Stark shift uncertainty (kHz)	Measurement uncertainty (kHz)	Total uncertainty (kHz)	Residual ( $\nu_m - \nu_c$ ) (kHz)
50	27.181 946	25	18	20	27	-11
49	28.962 156	22	16	20	25	2
48	30.901 335	19	14	20	24	-11
47	33.017 689	16	11	20	23	-7
46	35.331 922	14	10	20	22	9
45	37.867 714	12	8	20	21	19
40	54.981 702	23	7	90	90	32
39	59.590 806	20	6	40	40	9
38	64.730 288	16	5	50	50	-13
37	70.478 739	13	4	40	40	-51
36	76.929 284	11	3	40	40	-7
35	84.192 497	5	3	40	40	53
34	92.400 486	...	...	90	90	-11
33	101.712 394	...	...	70	70	-46

TABLE VII.  $4snp\ ^1P_1 \rightarrow 4sns\ ^3S_1$  transitions.

$n$	Transition frequency ( $\nu_m$ , GHz)	Stark shift (kHz)	Stark shift uncertainty (kHz)	Measurement uncertainty (kHz)	Total uncertainty (kHz)	Residual ( $\nu_m - \nu_c$ ) (kHz)
53	27.883 024	51	24	20	31	-2
52	29.598 363	45	21	20	29	-12
51	31.457 434	42	19	20	28	6
50	33.475 556	39	18	20	27	-3
49	35.670 175	33	15	20	25	9
48	38.060 978	29	13	20	24	0
43	53.865 611	14	6	40	40	10
42	58.036 052	12	5	40	40	3
41	62.648 682	10	4	800 <sup>a</sup>	800	0
40	67.763 730	8	4	40	40	-11
39	73.451 687	7	3	300 <sup>b</sup>	300	96
38	79.794 782	6	2	40	40	-3

<sup>a</sup>Anomalous line shapes (see Sec. III A).<sup>b</sup>See Sec. III A.TABLE VIII.  $4sns\ ^1S_0 \rightarrow 4snp\ ^3P_1$  transitions.

$n$	Transition frequency ( $\nu_m$ , GHz)	Stark shift (kHz)	Stark shift uncertainty (kHz)	Measurement uncertainty (kHz)	Total uncertainty (kHz)	Residual ( $\nu_m - \nu_c$ ) (kHz)
47	27.210 363	-95	45	15	47	2
46	29.114 227	-100	43	15	46	-8
45	31.199 936	-69	32	15	36	2
44	33.489 688	-50	23	15	28	-5
43	36.009 083	-42	20	15	25	0
42	38.787 640	-35	16	15	22	8
38	53.267 422	-17	8	30	31	0
37	57.983 645	-14	6	30	30	-32
36	63.273 489	-11	5	30	30	25
35	69.226 614	-9	4	200 <sup>a</sup>	200	-63
34	75.950 700	-8	3	30	30	47
33	83.574 209	-6	2	35	35	-50
32	92.253 121	-5	2	700 <sup>b</sup>	700	23
31	102.176 337	-4	1	700 <sup>b</sup>	700	113
30	113.574 810	-3	1	35	35	-4

<sup>a</sup>See Sec. III A.<sup>b</sup>Anomalous line shapes (see Sec. III A).TABLE IX.  $4snp\ ^1P_1 \rightarrow 4sn'd\ ^3D_1$  transitions.

$n$	Transition frequency ( $\nu_m$ , GHz)	Stark shift (kHz)	Stark shift uncertainty (kHz)	Measurement uncertainty (kHz)	Total uncertainty (kHz)	Residual ( $\nu_m - \nu_c$ ) (kHz)
$n' = n$						
52	53.337 893	232	111	50	121	-55
51	56.626 709	199	95	40	103	-38
50	60.191 586	170	81	40	90	8
$n' = n - 2$						
51	54.164 533	-143	68	40	79	-29
50	57.647 436	-118	56	40	69	-48
49	61.435 533	-101	48	40	62	13
48	65.562 847	-87	41	40	57	34
47	70.068 189	-74	35	50	61	-25
46	74.996 001	-63	30	40	50	-16
$n' = n - 1$						
25	28.090 784	...	...	20	20	-13
24	32.122 745	...	...	20	20	19
23	36.979 438	...	...	20	20	-5

TABLE X.  $4snp\ ^1P_1 \rightarrow 4sn'd\ ^3D_2$  transitions.

$n$	Transition frequency ( $\nu_m$ , GHz)	Stark shift (kHz)	Stark shift uncertainty (kHz)	Measurement uncertainty (kHz)	Total uncertainty (kHz)	Residual ( $\nu_m - \nu_c$ ) (kHz)
$n' = n$						
52	53.394 400	215	102	50	114	-59
51	56.686 605	184	88	40	96	-174
50	60.255 382	158	75	40	85	-50
$n' = n - 2$						
51	54.096 520	-135	64	40	75	-30
50	57.574 903	-111	53	40	66	-44
49	61.358 068	-96	45	50	67	32
48	65.479 862	-82	39	40	56	-65
47	69.979 353	-70	33	40	52	-48
46	74.900 668	-60	28	40	49	-35
$n' = n - 1$						
25	28.793 206	...	...	20	20	18
24	32.940 350	...	...	20	20	-30
23	37.940 550	...	...	20	20	10

TABLE XI.  $4snp\ ^1P_1 \rightarrow 4snd\ ^1D_2$  transitions.

$n$	Transition frequency ( $\nu_m$ , GHz)	Stark shift (kHz)	Stark shift uncertainty (kHz)	Measurement uncertainty (kHz)	Total uncertainty (kHz)
55	26.458 658	-158	118	30	122
54	28.056 406	-140	104	30	108
53	29.786 600	-122	91	30	96
52	31.663 227	-106	79	30	84
51	33.702 379	-98	73	30	79
50	35.922 164	-90	67	30	73
49	38.343 110	-77	57	30	65
44	54.423 341	-81	38	30	48
43	58.689 197	-72	34	30	45
42	63.418 575	-65	31	30	43
41	68.676 906	-55	26	30	40
40	74.541 084	-46	21	30	40
39	81.102 113	-38	18	60	62
38	88.467 721	-31	15	750 <sup>a</sup>	750
37	96.766 918	-28	13	1000 <sup>a</sup>	1000
36	106.154 122	-47	14	70	71
35	116.815 815	-39	12	50	51

<sup>a</sup>Anomalous line shapes (see Sec. III A).

TABLE XII.  $4snp\ ^1P_1 \rightarrow 4s(n-1)d\ ^1D_2$  transitions.

$n$	Transition frequency ( $\nu_m$ , GHz)	Stark shift (kHz)	Stark shift uncertainty (kHz)	Measurement uncertainty (kHz)	Total uncertainty (kHz)
47	27.030 859	51	38	30	48
46	28.746 717	43	32	30	44
45	30.603 788	66	49	30	57
44	32.615 848	58	43	30	53
43	34.797 899	53	39	30	49
42	37.166 474	41	31	30	43
41	39.739 667	37	28	30	41
36	56.415 896	21	10	30	32
35	60.678 519	17	8	750 <sup>a</sup>	750
34	65.306 738	14	6	750 <sup>a</sup>	750
33	70.321 013	11	5	750 <sup>a</sup>	750
32	75.735 449	9	4	100	100
31	81.553 891	7	3	60	60
30	87.762 623	...	...	1300 <sup>a</sup>	1300
29	94.320 870	...	...	1700 <sup>a</sup>	1700
28	101.145 168	...	...	1200 <sup>a</sup>	1200
27	108.089 681	...	...	100	100
26	114.914 544	...	...	100	100

<sup>a</sup>Anomalous lines shapes (see Sec. III A).

## APPENDIX B

TABLE XIII. Fitting parameters extracted from quantum-defect analysis of the data using the perturber form [Eq. (6)] for the  $4snp\ ^1P_1$  series. (See discussion in Sec. IV C.)

Series	Fitting parameters	Total uncertainty
$4snp\ ^1P_1$	$\delta_0 = 1.931\ 296\ 83$	0.005
	$\delta_1 = -2.301\ 167$	0.10
	$\alpha = 2.238\ 042\ 1 \times 10^{-3}$	$2.3 \times 10^{-4}$
$4sns\ ^1S_0$	$\delta_0 = 2.337\ 930\ 10$	$3 \times 10^{-6}$
	$\delta_1 = -0.114\ 241$	0.003
$4sns\ ^3S_1$	$\delta_0 = 2.440\ 955\ 58$	$3 \times 10^{-6}$
	$\delta_1 = 0.349\ 699$	0.003
$4snp\ ^3P_1$	$\delta_0 = 1.964\ 709\ 39$	$3 \times 10^{-6}$
	$\delta_1 = 0.227\ 687$	0.003
$4snd\ ^3D_1$	$\delta'_0 = 0.883\ 441\ 30$	$5 \times 10^{-4}$
	$\delta'_1 = -0.018\ 078$	0.04
	$\alpha = 8.528\ 297\ 9 \times 10^{-4}$	$9 \times 10^{-6}$
$4snd\ ^3D_2$	$\delta'_0 = 0.885\ 946\ 28$	$5 \times 10^{-4}$
	$\delta'_1 = 0.132\ 897$	0.04
	$\alpha = 9.091\ 600\ 6 \times 10^{-4}$	$9 \times 10^{-6}$

\*Present address: Kellogg Radiation Laboratory, California Institute of Technology, Pasadena, CA 91125.

†Present address: Science Research Laboratory, Inc., 15 Ward Street, Somerville, MA 02143.

<sup>1</sup>K. B. MacAdam and W. H. Wing, Phys. Rev. A **12**, 1464 (1975).

<sup>2</sup>T. F. Gallagher, R. M. Hill, and S. A. Edelstein, Phys. Rev. A **13**, 1448 (1976).

<sup>3</sup>C. Fabre, P. Goy, and S. Haroche, J. Phys. B **10**, L183 (1977).

<sup>4</sup>C. Fabre, S. Haroche, and P. Goy, Phys. Rev. A **22**, 778 (1980), and references therein.

<sup>5</sup>P. Goy, J. M. Raimond, G. Vitrant, and S. Haroche, Phys. Rev. A **26**, 2733 (1982).

<sup>6</sup>P. Goy, J. Liang, M. Gross, and S. Haroche, Phys. Rev. A **34**, 2889 (1986).

<sup>7</sup>A. Ganesh Vaidyanathan *et al.*, Phys. Rev. A **26**, 3346 (1982).

- <sup>8</sup>W. R. S. Garton and K. Codling, Proc. Phys. Soc. London **86**, 1067 (1965).
- <sup>9</sup>Gerd Risberg, Ark. Fys. **37**, 231 (1968).
- <sup>10</sup>C. M. Brown, S. G. Tilford, and M. L. Ginter, J. Opt. Soc. Am. **63**, 1454 (1973).
- <sup>11</sup>J. A. Armstrong, P. Esherick, and J. J. Wynne, Phys. Rev. A **15**, 180 (1977).
- <sup>12</sup>S. A. Borgström and J. R. Rubbmark, J. Phys. B **10**, 3607 (1977).
- <sup>13</sup>J. A. Armstrong, J. J. Wynne, and P. Esherick, J. Opt. Soc. Am. **69**, 211 (1979).
- <sup>14</sup>R. Beigang, K. Lücke, D. Schmidt, A. Timmerman, and P. J. West, Phys. Scr. **26**, 183 (1982).
- <sup>15</sup>Thomas R. Gentile, Barbara J. Hughey, Daniel Kleppner, and Theodore W. Ducas, Phys. Rev. A **40**, 5103 (1989).
- <sup>16</sup>A. G. Vaidyanathan, W. P. Spencer, and B. J. Hughey (unpublished).
- <sup>17</sup>Thomas R. Gentile, Ph.D. thesis, MIT, 1989.
- <sup>18</sup>R. M. Langer, Phys. Rev. **35**, 649 (1930).
- <sup>19</sup>Hans A. Bethe and Edwin E. Salpeter, *Quantum Mechanics of One- and Two-Electron Atoms* (Plenum, New York, 1977).
- <sup>20</sup>A. G. Shenstone and H. N. Russell, Phys. Rev. **39**, 415 (1932).
- <sup>21</sup>W. R. S. Garton, J. Quant. Spectrosc. Radiat. Transfer **2**, 335 (1962).
- <sup>22</sup>B. Edlen, in *Encyclopedia of Physics* (Springer, Berlin, 1964), Vol. XXVII, p. 136.
- <sup>23</sup>W. E. Cooke and C. L. Cromer, Phys. Rev. A **32**, 2725 (1985), and references therein.
- <sup>24</sup>Philip R. Bevington, *Data Reduction and Error Analysis for the Physical Sciences* (McGraw-Hill, New York, 1969), Chap. 11. The software used was C-PLOT™ (Certified Scientific Software, Cambridge, MA, 1988).
- <sup>25</sup>J. Sugar and C. Corliss, J. Phys. Chem. Ref. Data **14**, Suppl. 2, 51 (1985).